

Computer Stereo Vision for Autonomous Driving

Rui Fan*, Li Wang, Muhammad Junaid Bocus, Ioannis Pitas

Abstract For a long time, autonomous cars were found only in science fiction movies and series but now they are becoming a reality. The opportunity to pick such a vehicle at your garage forecourt is closer than you think. As an important component of autonomous systems, autonomous car perception has had a big leap with recent advances in parallel computing architectures, such as OpenMP for multi-threading CPUs and OpenCL for GPUs. With the use of tiny but full-feature embedded supercomputers, computer stereo vision has been prevalently applied in autonomous cars for depth perception. The two key aspects of computer stereo vision are speed and accuracy. They are two desirable but conflicting properties – the algorithms with better disparity accuracy usually have higher computational complexity. Therefore, the main aim of developing a computer stereo vision algorithm for resource-limited hardware is to improve the trade-off between speed and accuracy. In this chapter, we first introduce the autonomous car system, from the hardware aspect to the software aspect. We then discuss four autonomous car perception functionalities, including: 1) visual feature detection, description and matching, 2) 3D information acquisition, 3)

Rui Fan

UC San Diego, e-mail: rfan@ucsd.edu

Li Wang

ATG Robotics, e-mail: li.wang@ieee.org

Muhammad Junaid Bocus

University of Bristol, e-mail: junaid.bocus@bristol.ac.uk

Ioannis Pitas

Aristotle University of Thessaloniki, e-mail: pitas@csd.auth.gr

* Coresponding author

object detection/recognition and 4) semantic image segmentation. Finally, we introduce the principles of computer stereo vision and parallel computing.

1 Introduction

The autonomous car systems enable self-driving cars to navigate in complicated environments without any intervention of human drivers. An autonomous car system typically consists of two main parts [1]: 1) hardware and 2) software. An example of the autonomous car system architecture is illustrated in Fig 1. The hardware mainly includes 1) car sensors, such as cameras, lidars, and radars, and 2) car chassis, such as throttle, brake, and wheel. On the other hand, the software is comprised of four main modules (functional groups): 1) perception, 2) localization and mapping, 3) prediction and planning, and 4) control. Computer stereo vision is an important component of the perception module. It enables self-driving cars to perceive environments in 3D.

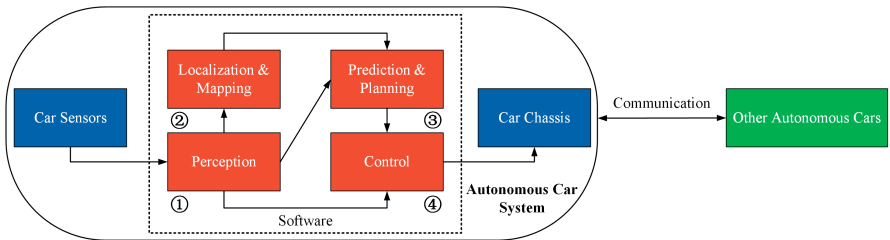


Fig. 1 Autonomous car system architecture.

This chapter first introduces the autonomous car system, from the hardware aspect (car sensors and car chassis) to the software aspect (perception, localization and mapping, prediction and planning, and control). Then, we discuss four autonomous car perception functionalities, including: 1) visual feature detection, description and matching, 2) 3D information acquisition, 3) object detection/recognition and 4) semantic image segmentation. Finally, the principles of computer stereo vision and parallel computing on both CPU and GPU are detailed.

2 Autonomous Car System

2.1 Hardware

2.1.1 Car Sensors

When choosing car sensors, we need to consider many different factors, such as sampling rate, field of view (FoV), accuracy, range, cost and overall system complexity¹. The most commonly used car sensors include: a) passive sensors, such as cameras; b) active sensors, such as lidars, radars and ultrasonic transceivers; and other types of sensors, such as global positioning systems (GPS), inertial measurement unit (IMU), among others.

Cameras capture 2D images by collecting light reflected on 3D objects. The images captured from different views can be utilized to reconstruct the 3D geometry of the driving scene. The perspective (or pinhole) camera model and the mathematical principle of multi-view geometry will be discussed in Section 4. Furthermore, most autonomous car perception tasks, such as semantic driving scene segmentation and object detection/recognition, are developed for images. In Section 3, we provide readers with a comprehensive overview of these tasks. However, the image quality is always subject to environmental conditions, such as weather and illumination [2]. Therefore, the visual information from other sensors is typically required for robust autonomous car perception.

Lidar illuminates a target with pulsed laser light and measures the source distance to the target by analyzing the reflected laser pulses [3]. Due to its ability to generate highly accurate 3D geometry model, lidars are generally mounted on autonomous cars for depth perception. For example, current industrial autonomous car localization and mapping systems are generally based on lidars. Furthermore, radars can measure both the range and radial velocity of an object by transmitting an electromagnetic wave and analyzing its reflections [4]. Radars are already established in the automotive industry, and they have been prevalently employed in intelligent vehicles to enable advanced driver assistance system (ADAS) features, such as adaptive cruise control and autonomous emergency braking¹. Similar to Radar, ultrasonic transducers calculate the distance to an object by measuring the time between transmitting an ultrasonic signal and receiving its echo [5]. Ultrasonic transducers are commonly used for autonomous car localization and navigation.

¹ autonomous-driving.org/2019/01/25/positioning-sensors-for-autonomous-vehicles/

In addition to the aforementioned passive and active sensors, GPS and IMU are commonly used to enhance the performance of the localization and mapping module in autonomous car systems [6]. GPS can provide both time and geolocation information for autonomous cars, but its signals can become very weak when they are blocked by obstacles, *e.g.*, buildings, which result in GPS-denied regions [7]. Hence, the integration of GPS and IMU is widely adopted to provide continuous position and velocity information for autonomous cars [6].

2.1.2 Car Chassis

Car chassis technologies, especially drive-by-wire (DbW), are required for building autonomous vehicles. DbW technology refers to the electronic systems that replace traditional mechanical controls [8]. DbW can perform vehicle functions, which are traditionally achieved by mechanical linkages, through electrical or electro-mechanical systems. There are three main vehicle control systems that are commonly replaced with electronic controls: 1) throttle, 2) braking, and 3) steering.

A throttle-by-wire (TbW) system helps accomplish vehicle propulsion via an electronic throttle, without any cables from the accelerator pedal to the throttle valve of the engine. In electric vehicles, the TbW system controls the electric motors by sensing the accelerator pedal input and sending signal to the power inverter modules. Compared to traditional hydraulic brakes, which provide braking effort by building hydraulic pressure in the brake lines, a brake-by-wire (BbW) system completely eliminates the need for hydraulics by using electronic motors to activate calipers. Furthermore, in the vehicles that are equipped with steer-by-wire (SbW) technology, there is no physical connection between the steering wheel and the tires. The control of the wheels' direction will be established through electric motor(s), which are actuated by electronic control units monitoring the steering wheel inputs.

In comparison to traditional throttle systems, electronic throttle systems are much lighter, greatly reducing the weight of modern cars. In addition, they are easier to service and tune, as a technician can simply connect a laptop to perform the tuning. Moreover, an electronic control system allows more accurate control of the throttle opening compared to a cable that stretches over time. Furthermore, since the steering wheel can be bypassed as an input device, safety can be improved by providing computer controlled intervention of vehicle controls with systems, such as adaptive cruise control and electronic stability control.

2.2 Software

The perception module analyzes the raw data collected by the car sensors (see section 2.1.1) and outputs its understanding to the environment. This process is similar to human visual cognition. We discuss different autonomous car perception tasks in section 3.

The outputs from the perception module are then used by other modules. The localization and mapping module not only estimates the autonomous car location, but also constructs and updates the environmental map [9]. This topic has become very popular since the concept of *simultaneous localization and mapping (SLAM)* was introduced in 1986 [10].

The prediction and planning module first analyzes the motion patterns of other traffic agents and predicts their future trajectories. Such prediction outputs are then used to determine possible safe navigation routes for the autonomous vehicle [11] using different path planning techniques, such as Dijkstra [12], A-star (or simply A*) [13], *etc.*

Finally, the control module sends appropriate commands to the car controllers (see section 2.1.2) based on the predicted trajectory as well as the estimated vehicle states, which enables the autonomous vehicle to follow the planned trajectory as closely as possible. Traditional controllers, such as proportional-integral-derivative (PID) [14], linear-quadratic regulator (LQR) [15] and model predictive control (MPC) [16] are still the most commonly used ones in autonomous car control module.

3 Autonomous Car Perception

The autonomous car perception module has four main functionalities:

1. visual feature detection, description and matching;
2. 3D information acquisition;
3. objection detection/recognition;
4. semantic image segmentation.

Since the 21st century, visual feature detectors and descriptors have become very popular research topics in the computer vision and robotics communities. They have been prevalently employed in many applications [17], such as image classification [18], 3D scene reconstruction [19], object recognition [20] and visual

tracking [21]. The matched visual feature correspondences between two (or more) images can be utilized to establish the relationships among a collection of images [17]. The most well-known visual feature detection, description and matching algorithms include: scale-invariant feature transform (SIFT) [22], speeded up robust feature (SURF) [23], oriented FAST and rotated BRIEF (ORB) [24], binary robust invariant scalable keypoints (BRISK) [25], and so forth.

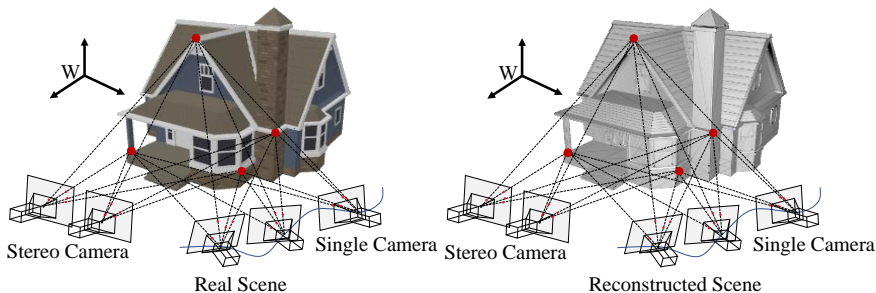


Fig. 2 3D scene reconstruction, where W presents the world coordinate system (WCS).

The digital images captured by cameras are essentially 2D. In order to extrapolate the 3D information from a given scene, the images from multiple views are required [26]. These images can be captured using either a single movable camera [27] or an array of synchronized cameras, as shown in Fig. 2. The former is typically known as *structure from motion (SfM)* [28] or *optical flow* [27], while the latter is typically referred to as *stereo vision* or *binocular vision* [29]. SfM methods estimate camera poses and the 3D points of interest from images captured from multiple views, which are linked by a collection of visual features. They also leverage bundle adjustment (BA) [30] technique to refine the estimated camera poses and the 3D point locations by minimizing a cost function known as total reprojection error. Optical flow describes the motion of pixels between consecutive frames of a video sequence [31], and it is regarded as an effective tool for dynamic object detection [27]. Stereo vision acquires the depth information by comparing the horizontal positional differences (disparities) of the correspondence pairs between two synchronously captured images. More details on computer stereo vision will be given in Section 4.3.

Object detection/recognition is a computer vision technique for identifying particular objects in images/videos [32]. It typically performs different subtasks, such as pedestrian detection [33], vehicle detection [31], traffic sign detection [34], cyclist detection [35], *etc.*, as shown in Fig. 3. The existing object detection approaches can be classified as either computer vision-based or machine/deep



Fig. 3 Object detection.

learning-based. The former typically consists of three steps [32]: 1) informative region selection (scanning the whole image by sliding windows with particular templates to produce candidate regions); 2) visual feature extraction, as discussed above; and 3) object classification (distinguishing a target object from all the other categories using a classifier). With recent advances in machine/deep learning, a large number of convolutional neural networks (CNNs) have been proposed to recognize objects from images/videos, and these approaches have achieved very impressive results. The most popular ones include: regions with CNN features (R-CNN) [36], fast R-CNN [37], faster R-CNN [38], you only look once (YOLO) [39], YOLOv3 [40], YOLOv4 [41], *etc.*

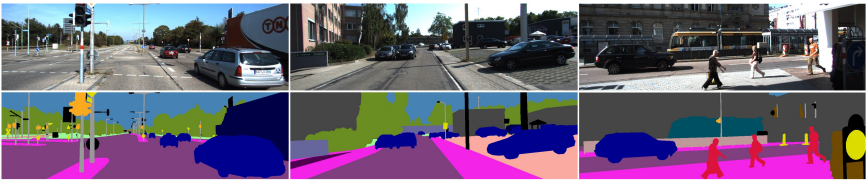


Fig. 4 Semantic image segmentation.

Semantic image segmentation labels every pixel in the image with a given object class [42], such as lane marking, vehicle, collision-free space, and pedestrian, as illustrated in Fig. 4. The state-of-the-art semantic image segmentation approaches are mainly categorized into two main groups [43]: 1) single-modal and 2) data-fusion. The former typically segments RGB images with an encoder-decoder CNN architecture. In recent years, many popular single-model semantic image segmentation algorithms, such as fully convolutional network (FCN) [44], U-Net [45], SegNet [46], DeepLabv3+ [47], DenseASPP [48], DUpsampling [49], *etc.*, have been presented in computer vision community. On the other hand, data-fusion semantic image segmentation approaches generally extract features from two different types of vision data [50], such as RGB and depth images in FuseNet [51], RGB and surface normal images [52] in SNE-RoadSeg [42], RGB and transformed disparity images [53–55] in AA-RTFNet [50], or RGB and ther-

mal images in MFNet [56]. The extracted feature maps are then fused to provide a better semantic prediction.

Please note: a given autonomous car perception task can sometimes be solved by different types of functionalities. For instance, lane marking detection can be formulated as a linear/quadratic/quadruplicate pattern recognition problem and solved by straight line detection algorithms [57] or dynamic programming algorithms [58–60]. On the other hand, it can also be formulated as a semantic image segmentation problem and solved by CNNs.

4 Computer Stereo Vision

4.1 Preliminaries

1. Skew-symmetric matrix

In linear algebra, a *skew-symmetric matrix* \mathbf{A} satisfies the following property: its transpose is identical to its negative, *i.e.*, $\mathbf{A}^T = -\mathbf{A}$. In 3D computer vision, the skew-symmetric matrix $[\mathbf{a}]_{\times}$ of a vector $\mathbf{a} = [a_1, a_2, a_3]^T$ can be written as [26]:

$$[\mathbf{a}]_{\times} = \begin{bmatrix} 0 & -a_3 & a_2 \\ a_3 & 0 & -a_1 \\ -a_2 & a_1 & 0 \end{bmatrix}. \quad (1)$$

A skew-symmetric matrix has two important properties:

$$\mathbf{a}^T [\mathbf{a}]_{\times} = \mathbf{0}^T, \quad [\mathbf{a}]_{\times} \mathbf{a} = \mathbf{0}, \quad (2)$$

where $\mathbf{0} = [0, 0, 0]^T$ is a zero vector. Furthermore, the cross product of two vectors \mathbf{a} and \mathbf{b} can be formulated as a matrix multiplication process [26]:

$$\mathbf{a} \times \mathbf{b} = [\mathbf{a}]_{\times} \mathbf{b} = -[\mathbf{b}]_{\times} \mathbf{a}. \quad (3)$$

These properties are generally used to simplify the equations related to vector cross-product.

2. Lie group $SO(3)$ and $SE(3)$

A 3D point $\mathbf{x}_1 = [x_1, y_1, z_1]^T$ can be transformed into another 3D point $\mathbf{x}_2 = [x_2, y_2, z_2]^T$ using a rotation (orthogonal) matrix $\mathbf{R} \in \mathbb{R}^{3 \times 3}$ and a translation

vector $\mathbf{t} \in \mathbb{R}^{3 \times 1}$:

$$\mathbf{x}_2 = \mathbf{R}\mathbf{x}_1 + \mathbf{t}, \quad (4)$$

where \mathbf{R} satisfies:

$$\mathbf{R}\mathbf{R}^\top = \mathbf{R}^\top\mathbf{R} = \mathbf{I} \quad \text{and} \quad |\det(\mathbf{R})| = 1. \quad (5)$$

\mathbf{I} is an identity matrix and $\det(\mathbf{R})$ represents the determinant of \mathbf{R} . The group containing all rotation matrices is referred to as a *special orthogonal group* and is denoted as $SO(3)$. \mathbf{x}_1 and \mathbf{x}_2 are related to each other as follows:

$$\tilde{\mathbf{x}}_2 = \mathbf{P}\tilde{\mathbf{x}}_1, \quad (6)$$

where

$$\mathbf{P} = \begin{bmatrix} \mathbf{R} & \mathbf{t} \\ \mathbf{0}^\top & 1 \end{bmatrix}, \quad (7)$$

$\tilde{\mathbf{x}}_1 = [\mathbf{x}_1^\top, 1]^\top$ and $\tilde{\mathbf{x}}_2 = [\mathbf{x}_2^\top, 1]^\top$ denote the homogeneous coordinates of \mathbf{x}_1 and \mathbf{x}_2 , respectively. \mathbf{P} is a homogeneous transformation matrix². The group containing all homogeneous transformation matrices is referred to as a *special Euclidean group* and is denoted as $SE(3)$.

4.2 Multi-View Geometry

4.2.1 Perspective Camera Model

The perspective (or pinhole) camera model, as illustrated in Fig. 5, is the most common geometric model used to describe the relationship between a 3D point $\mathbf{p}^C = [x^C, y^C, z^C]^\top$ in the camera coordinate system (CCS) and its projection $\bar{\mathbf{p}} = [x, y, f]^\top$ on the image plane Π . \mathbf{o}^C is the camera center. The distance between Π and \mathbf{o}^C is the camera focal length f . $\hat{\mathbf{p}}^C = [\frac{x^C}{z^C}, \frac{y^C}{z^C}, 1]^\top$ is the normalized coordinates of $\mathbf{p}^C = [x^C, y^C, z^C]^\top$. The ray originating from \mathbf{o}^C and passing perpendicularly through Π is known as the optical axis. The relationship between \mathbf{p}^C and $\bar{\mathbf{p}}$ is as follows [61]:

$$\bar{\mathbf{p}} = f\hat{\mathbf{p}}^C = \frac{f}{z^C}\mathbf{p}^C. \quad (8)$$

² www.seas.upenn.edu/~meam620/slides/kinematicsI.pdf

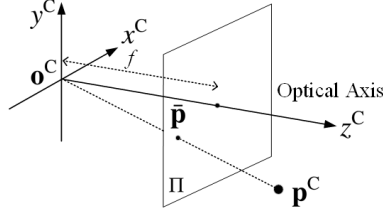


Fig. 5 Perspective camera model. A 3D point \mathbf{p}^C in the CCS is projected at $\bar{\mathbf{p}}$ on the image plane Π . Their transformation can be realized using (8).

4.2.2 Intrinsic Matrix

Since the lens distortion does not exist in a perspective camera model, $\bar{\mathbf{p}} = [x, y, f]^T$ on the image plane Π can be transformed into a pixel $\mathbf{p} = [u, v]^T$ in the image using [29]:

$$u = u_o + s_x x, \quad v = v_o + s_y y, \quad (9)$$

where $\mathbf{p}_o = [u_o, v_o]^T$ is the principal point, and s_x and s_y are the effective size measured (in pixels per millimeter) in the horizontal and vertical directions, respectively [61]. To simplify the expression of the intrinsic matrix \mathbf{K} , two notations $f_x = f s_x$ and $f_y = f s_y$ are introduced. u_o, v_o, f, s_x and s_y [26] are five intrinsic parameters. Combining (8) and (9), a 3D point \mathbf{p}^C in the CCS can be transformed into a pixel \mathbf{p} in the image using [62]:

$$\bar{\mathbf{p}} = \frac{1}{z^C} \mathbf{K} \mathbf{p}^C = \frac{1}{z^C} \begin{bmatrix} f_x & 0 & u_o \\ 0 & f_y & v_o \\ 0 & 0 & 1 \end{bmatrix} \begin{bmatrix} x^C \\ y^C \\ z^C \end{bmatrix}, \quad (10)$$

where $\tilde{\mathbf{p}} = [\mathbf{p}^T, 1]^T = [u, v, 1]^T$ denotes the homogeneous coordinates of $\mathbf{p} = [u, v]^T$. Plugging (10) into (8) results in:

$$\hat{\mathbf{p}}^C = \mathbf{K}^{-1} \tilde{\mathbf{p}} = \frac{\bar{\mathbf{p}}}{f} = \frac{\mathbf{p}^C}{z^C}. \quad (11)$$

Therefore, an arbitrary 3D point lying on the ray, which goes from \mathbf{o}^C and through \mathbf{p}^C , is always projected at $\bar{\mathbf{p}}$ on the image plane.

4.2.3 Lens Distortion

In order to get better imaging results, a lens is usually installed in front of the camera [61]. However, this introduces distortions to the images. The optical aberration caused by the installed lens typically deforms the physically straight lines and makes them appear as curves in the images [63], as shown in Fig. 6(a).



Fig. 6 Distorted image correction: (a) original image; (b) corrected image.

The lens distortion has two main categories: 1) radial distortion and 2) tangential distortion [29]. The presence of radial distortion is due to the fact that lens's geometric shape affects the straight line transmission, while the tangential distortion occurs because the lens installed in front of the camera is not perfectly parallel to the image plane [61]. In practical experiments, the image geometry is affected to a much higher extent with radial distortion than with tangential distortion, and therefore, the latter is sometimes neglected in the process of distorted image correction.

Radial distortion

The radial distortion mainly includes 1) barrel distortion, 2) pincushion distortion and 3) mustache distortion. An example of each type is shown in Fig. 7.

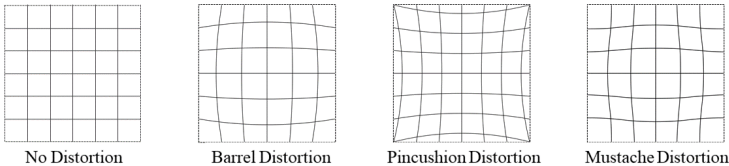


Fig. 7 Lens distortion types.

It can be observed from the distorted images that the radial distortions are symmetric about the image center and the lines are no longer straight. In barrel distortion, the image magnification decreases with the distance from the optical

axis (lines curve outwards). In contrast, the pincushion distortion pinches the image (lines curve inwards). Mustache distortion is a mixture of the above two types. It starts out as barrel distortion close to the optical axis and gradually turns into pincushion distortion towards the image periphery. Barrel distortion is commonly applied in fish-eye lenses to produce wide-angle/panoramic images, while pincushion distortion is often associated with telephoto lenses to eliminate the globe effects.

Radial distortions can be corrected using³:

$$\begin{aligned} x_{\text{undist}} &= x_{\text{dist}}(1 + k_1 r^2 + k_2 r^4 + k_3 r^6), \\ y_{\text{undist}} &= y_{\text{dist}}(1 + k_1 r^2 + k_2 r^4 + k_3 r^6), \end{aligned} \quad (12)$$

where $x_{\text{dist}} = \frac{x^C}{z^C} = \frac{u-u_0}{f_x}$ and $y_{\text{dist}} = \frac{y^C}{z^C} = \frac{v-v_0}{f_y}$ are obtained from the distorted image; the corrected point will be $\mathbf{p}_{\text{undist}} = [x_{\text{undist}}, y_{\text{undist}}]^T$; $r^2 = x_{\text{dist}}^2 + y_{\text{dist}}^2$. k_1 , k_2 and k_3 are three intrinsic parameters used for radial distortion correction, and they can be estimated using a collection of images containing a planar checkerboard pattern.

Tangential distortion

Similar to the radial distortion, the tangential distortion can also be corrected using:

$$\begin{aligned} x_{\text{undist}} &= x_{\text{dist}} + [2p_1 x_{\text{dist}} y_{\text{dist}} + p_2 (r^2 + 2x_{\text{dist}}^2)], \\ y_{\text{undist}} &= y_{\text{dist}} + [p_1 (r^2 + 2y_{\text{dist}}^2) + 2p_2 x_{\text{dist}} y_{\text{dist}}], \end{aligned} \quad (13)$$

where p_1 and p_2 are two intrinsic parameters, which can also be estimated using a collection of images containing a planar checkerboard pattern. As shown in Fig. 6(b), we can observe that the bent checkerboard grids become straight when the lens distortion is corrected.

³ docs.opencv.org/2.4/doc/tutorials/calib3d/camera_calibration/camera_calibration.html

⁴ docs.opencv.org/2.4/modules/imgproc/doc/geometric_transformations.html

4.2.4 Epipolar Geometry

The generic geometry of stereo vision is known as *epipolar geometry*. An example of the epipolar geometry is shown in Fig. 8, where Π_L and Π_R represent the

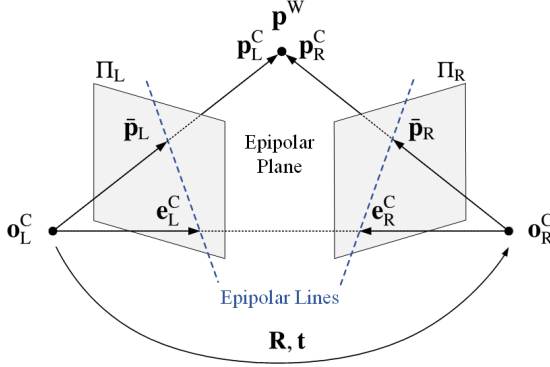


Fig. 8 Epipolar geometry. A 3D point \mathbf{p}_L^C in the LCCS is transformed to \mathbf{p}_R^C in the RCCS using (14).

left and right image planes, respectively; \mathbf{o}_L^C and \mathbf{o}_R^C denote the origins of the left camera coordinate system (LCCS) and the right camera coordinate system (RCCS), respectively; $\mathbf{p}^W = [x^W, y^W, z^W]^T$, a 3D point in the WCS, is projected at $\tilde{\mathbf{p}}_L = [x_L, y_L, f_L]^T$ on Π_L and at $\tilde{\mathbf{p}}_R = [x_R, y_R, f_R]^T$ on Π_R , respectively; f_L and f_R are the focal lengths of the left and right cameras, respectively; The representations of \mathbf{p}^W in the LCCS and RCCS are $\mathbf{p}_L^C = [x_L^C, y_L^C, z_L^C]^T = \frac{z_L^C}{f_L} \tilde{\mathbf{p}}_L$ and $\mathbf{p}_R^C = [x_R^C, y_R^C, z_R^C]^T = \frac{z_R^C}{f_R} \tilde{\mathbf{p}}_R$, respectively. According to (4), \mathbf{p}_L^C can be transformed into \mathbf{p}_R^C using:

$$\mathbf{p}_R^C = \mathbf{R}\mathbf{p}_L^C + \mathbf{t}, \quad (14)$$

where $\mathbf{R} \in \mathbb{R}^{3 \times 3}$ is a rotation matrix and $\mathbf{t} \in \mathbb{R}^{3 \times 1}$ is a translation vector. \mathbf{e}_L^C and \mathbf{e}_R^C denote the left and right *epipoles*, respectively. The plane identified by \mathbf{o}_L^C , \mathbf{o}_R^C and \mathbf{p}^W is known as an *epipolar plane*, which intersects Π_L and Π_R in two lines. Such lines are generally referred to as *epipolar lines*. Using (11), \mathbf{p}_L^C and \mathbf{p}_R^C can be normalized:

$$\hat{\mathbf{p}}_L^C = \frac{\mathbf{p}_L^C}{z_L^C} = \mathbf{K}_L^{-1} \tilde{\mathbf{p}}_L, \quad \hat{\mathbf{p}}_R^C = \frac{\mathbf{p}_R^C}{z_R^C} = \mathbf{K}_R^{-1} \tilde{\mathbf{p}}_R, \quad (15)$$

where \mathbf{K}_L and \mathbf{K}_R denote the intrinsic matrices of the left and right cameras, respectively. $\tilde{\mathbf{p}}_L = [\mathbf{p}_L^T, 1]^T$ and $\tilde{\mathbf{p}}_R = [\mathbf{p}_R^T, 1]^T$ are the homogeneous coordinates of the image pixels $\mathbf{p}_L = [u_L, v_L]^T$ and $\mathbf{p}_R = [u_R, v_R]^T$, respectively.

4.2.5 Essential Matrix

Essential matrix $\mathbf{E} \in \mathbb{R}^{3 \times 3}$ was first introduced by Longuet-Higgins in 1981 [64]. A simple way of introducing the defining equation of \mathbf{E} is to multiply $\mathbf{p}_R^{C\top} [\mathbf{t}]_{\times}$ on both sides of (14) to obtain the following expression:

$$\mathbf{p}_R^{C\top} [\mathbf{t}]_{\times} \mathbf{p}_R^C = \mathbf{p}_R^{C\top} [\mathbf{t}]_{\times} (\mathbf{R} \mathbf{p}_L^C + \mathbf{t}). \quad (16)$$

According to (3), (16) can be rewritten as follows:

$$-\mathbf{p}_R^{C\top} [\mathbf{p}_R^C]_{\times} \mathbf{t} = \mathbf{p}_R^{C\top} [\mathbf{t}]_{\times} \mathbf{R} \mathbf{p}_L^C + \mathbf{p}_R^{C\top} [\mathbf{t}]_{\times} \mathbf{t}. \quad (17)$$

Applying (2) to (17) yields:

$$\mathbf{p}_R^{C\top} [\mathbf{t}]_{\times} \mathbf{R} \mathbf{p}_L^C = \mathbf{p}_R^{C\top} \mathbf{E} \mathbf{p}_L^C = 0, \quad (18)$$

where the essential matrix \mathbf{E} is defined as $\mathbf{E} = [\mathbf{t}]_{\times} \mathbf{R}$. Plugging (15) into (18) results in:

$$\hat{\mathbf{p}}_R^{C\top} \mathbf{E} \hat{\mathbf{p}}_L^C = 0, \quad (19)$$

which depicts the relationship between each pair of normalized points $\hat{\mathbf{p}}_R^C$ and $\hat{\mathbf{p}}_L^C$ lying on the same epipolar plane. It is important to note here that \mathbf{E} has five degrees of freedom (both \mathbf{R} and \mathbf{t} have three degrees of freedom, but the overall scale ambiguity causes the degrees of freedom to be reduced by one) [26]. Hence in theory, \mathbf{E} can be estimated with at least five pairs of \mathbf{p}_L^C and \mathbf{p}_R^C . However, due to the non-linearity of \mathbf{E} , its estimation using five pairs of correspondences is always intractable. Therefore, \mathbf{E} is commonly estimated with at least eight pairs of \mathbf{p}_L^C and \mathbf{p}_R^C [61]. The algorithm for estimating \mathbf{E} will be discussed in Section 4.2.6.

4.2.6 Fundamental Matrix

As introduced in Section 4.2.5, the essential matrix creates a link between a given pair of 3D correspondence points in the LCCS and RCCS. When the intrinsic matrices of the two cameras in a stereo rig are unknown, the relationship between each pair of 2D correspondence image pixels $\mathbf{p}_L = [u_L, v_L]^T$ and $\mathbf{p}_R = [u_R, v_R]^T$ can also be established. This relates to a *fundamental matrix* $\mathbf{F} \in \mathbb{R}^{3 \times 3}$. It can be considered as a generalization of \mathbf{E} , where the assumption of calibrated cameras is removed [26]. Applying (15) to (19) yields:

$$\tilde{\mathbf{p}}_R^\top \mathbf{K}_R^{-\top} \mathbf{E} \mathbf{K}_L^{-1} \tilde{\mathbf{p}}_L = \tilde{\mathbf{p}}_R^\top \mathbf{F} \tilde{\mathbf{p}}_L = 0, \quad (20)$$

where the fundamental matrix \mathbf{F} is defined as: $\mathbf{F} = \mathbf{K}_R^{-\top} \mathbf{E} \mathbf{K}_L^{-1}$. \mathbf{F} has seven degrees of freedom: a 3×3 homogeneous matrix has eight independent ratios (there are nine elements, and the common scaling is not significant); however, \mathbf{F} also satisfies the constraint $\det(\mathbf{F}) = 0$ which removes one degree of freedom [26]. The most commonly used algorithm to estimate \mathbf{E} and \mathbf{F} is “eight-point algorithm” (EPA), which was introduced by Hartley in 1997 [65]. This algorithm is based on the scale invariance of \mathbf{E} and \mathbf{F} , *i.e.*, $\lambda_{\mathbf{E}} \mathbf{p}_R^{\mathbf{C}\top} \mathbf{E} \mathbf{p}_L^{\mathbf{C}} = 0$ and $\lambda_{\mathbf{F}} \tilde{\mathbf{p}}_R^\top \mathbf{F} \tilde{\mathbf{p}}_L = 0$, where $\lambda_{\mathbf{E}}, \lambda_{\mathbf{F}} \neq 0$. By setting one element in \mathbf{E} and \mathbf{F} to 1, eight unknown elements still need to be estimated. This can be done using at least eight pairs of correspondences. If the intrinsic matrices \mathbf{K}_L and \mathbf{K}_R of the two cameras are known, the EPA only needs to be carried out once to estimate either \mathbf{E} or \mathbf{F} , because the other one can be easily worked out using (20).

4.2.7 Homography Matrix

For an arbitrary 3D point $\mathbf{p}^W = [x^W, y^W, z^W]^\top$ lying on a planar surface $\mathbf{n}^\top \mathbf{p}^W + b = 0$, where $\mathbf{n} = [n_x, n_y, n_z]^\top$ is the normal vector of the planar surface, its corresponding pixels $\mathbf{p}_L = [u_L, v_L]^\top$ and $\mathbf{p}_R = [u_R, v_R]^\top$ in the left and right images can be linked by a *homography matrix* $\mathbf{H} \in \mathbb{R}^{3 \times 3}$. The expression of the planar surface can be rearranged as follows:

$$-\mathbf{n}^\top \mathbf{p}^W / b = 1. \quad (21)$$

Assuming that $\mathbf{p}_L^{\mathbf{C}} = \mathbf{p}^W$ and plugging (21) and (15) into (14) results in:

$$\mathbf{p}_R^{\mathbf{C}} = \mathbf{R} \mathbf{p}_L^{\mathbf{C}} - \frac{1}{b} \mathbf{t} \mathbf{n}^\top \mathbf{p}_L^{\mathbf{C}} = \left(\mathbf{R} - \frac{1}{b} \mathbf{t} \mathbf{n}^\top \right) z_L^{\mathbf{C}} \mathbf{K}_L^{-1} \tilde{\mathbf{p}}_L = z_R^{\mathbf{C}} \mathbf{K}_R^{-1} \tilde{\mathbf{p}}_R \quad (22)$$

Therefore, $\tilde{\mathbf{p}}_L$ and $\tilde{\mathbf{p}}_R$ can be linked using:

$$\tilde{\mathbf{p}}_R = \frac{z_L^{\mathbf{C}}}{z_R^{\mathbf{C}}} \mathbf{K}_R \left(\mathbf{R} - \frac{1}{b} \mathbf{t} \mathbf{n}^\top \right) \mathbf{K}_L^{-1} \tilde{\mathbf{p}}_L = \mathbf{H} \tilde{\mathbf{p}}_L. \quad (23)$$

The homography matrix \mathbf{H} is generally used to distinguish obstacles from a planar surface. For a well-calibrated stereo vision system, \mathbf{R} , \mathbf{t} , \mathbf{K}_L as well as \mathbf{K}_R are already known, and $z_L^{\mathbf{C}}$ is typically equal to $z_R^{\mathbf{C}}$. Thus, \mathbf{H} only relates to \mathbf{n} and b , and it can be estimated with at least four pairs of correspondences \mathbf{p}_L and \mathbf{p}_R [66].

4.3 Stereopsis

4.3.1 Stereo Rectification

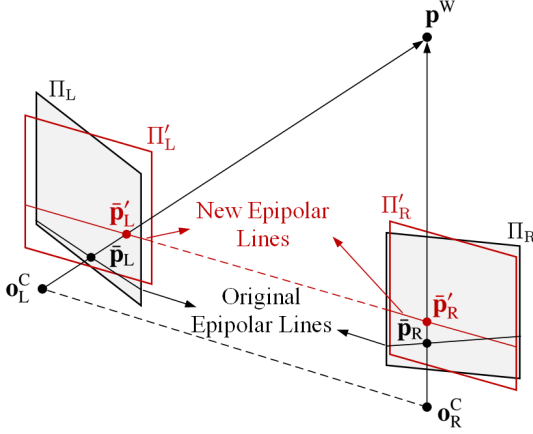


Fig. 9 stereo rectification: Π_L and Π_R represent the original left and right image planes, respectively; p_L and p_R are the projections of p^W on Π_L and Π_R , respectively; Π'_L and Π'_R denote the rectified left and right image planes, respectively; p'_L and p'_R are the projections of p^W on Π'_L and Π'_R , respectively.

The main task of 3D reconstruction with a pair of synchronized cameras is to determine each pair of correspondence pixels between the left and right images. For an uncalibrated stereo rig, finding the correspondence pairs is a 2D search process (optical flow estimation), which is extremely computationally intensive. Therefore, an image transformation process, referred to as *stereo rectification*, is always performed beforehand to reduce the dimension of the correspondence pair search. The stereo rectification consists of four main steps [61]:

1. Rotate the left camera by \mathbf{R}_{rect} so that the left image plane is parallel to the vector \mathbf{t} ;
2. Apply the same rotation to the right camera to recover the original epipolar geometry;
3. Rotate the right camera by \mathbf{R}^{-1} ;
4. Adjust the left and right image scales by allocating an identical intrinsic matrix to both cameras.

After the stereo rectification, the left and right images appear as if they were taken by a pair of parallel cameras with the same intrinsic parameters, as shown

in Fig. 9, where Π_L and Π_R are the original image planes; Π'_L and Π'_R are the rectified image planes. Also, each pair of conjugate epipolar lines become collinear and parallel to the horizontal image axis [61]. Hence, determining the correspondence pairs is simplified to a 1D search problem.

4.3.2 Stereo Vision System

A well-rectified stereo vision system is illustrated in Fig. 10, which can be re-

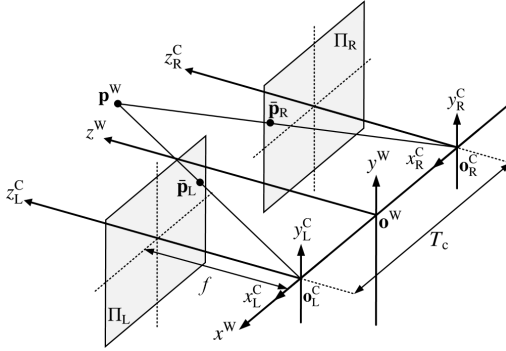


Fig. 10 Basic stereo vision system. \mathbf{p}^W can be transformed to $\bar{\mathbf{p}}_L^C$ and $\bar{\mathbf{p}}_R^C$ using (26).

garded as a specialization of the epipolar geometry introduced in Section 4.2.4, where the left and right cameras are perfectly parallel to each other; the x_L^C and x_R^C axes are collinear; \mathbf{o}_L^C and \mathbf{o}_R^C are the focuses of the left and right cameras, respectively; T_c , the baseline of the stereo rig, is defined as the distance between \mathbf{o}_L^C and \mathbf{o}_R^C ;

$$\mathbf{K}_L = \mathbf{K}_R = \mathbf{K} = \begin{bmatrix} f & 0 & u_o \\ 0 & f & v_o \\ 0 & 0 & 1 \end{bmatrix} \quad (24)$$

are the intrinsic matrices of the left and right cameras, respectively; $\mathbf{p}^W = [x^W, y^W, z^W]^T$ is a 3D point of interest in the WCS. Its representations in the LCCS and RCCS are $\mathbf{p}_L^C = [x_L^C, y_L^C, z_L^C]^T$ and $\mathbf{p}_R^C = [x_R^C, y_R^C, z_R^C]^T$, respectively. Since the left and right cameras are considered to be exactly the same in a well-rectified stereo vision system, s_x and s_y in (9) are simply set to 1 and $f_x = f_y = f$. \mathbf{p}^W is projected on Π_L at $\bar{\mathbf{p}}_L = [x_L, y_L, f]^T$ and on Π_R at $\bar{\mathbf{p}}_R = [x_R, y_R, f]^T$, respectively. \mathbf{o}^W , the origin of the WCS, is at the center of the line segment $L = \{t\mathbf{o}_L^C + (1-t)\mathbf{o}_R^C \mid t \in [0, 1]\}$. The z^W axis is perpendicular to Π_L and Π_R .

Therefore, an arbitrary point \mathbf{p}^W in the WCS can be transformed to \mathbf{p}_L^C and \mathbf{p}_R^C using:

$$\mathbf{p}_L^C = \mathbf{I}\mathbf{p}^W + \mathbf{t}_L, \quad \mathbf{p}_R^C = \mathbf{I}\mathbf{p}^W + \mathbf{t}_R, \quad (25)$$

where $\mathbf{t}_L = [\frac{T_c}{2}, 0, 0]^\top$ and $\mathbf{t}_R = [-\frac{T_c}{2}, 0, 0]^\top$; Applying (11) and (15) to (25) results in the following expressions:

$$\begin{aligned} x_L &= f \frac{x^W + T_c/2}{z^W}, & y_L &= f \frac{y^W}{z^W}, \\ x_R &= f \frac{x^W - T_c/2}{z^W}, & y_R &= f \frac{y^W}{z^W}. \end{aligned} \quad (26)$$

Applying (26) to (9) yields the following expressions:

$$\mathbf{p}_L = \begin{bmatrix} u_L \\ v_L \end{bmatrix} = \begin{bmatrix} f \frac{x^W}{z^W} + u_o + f \frac{T_c}{2z^W} \\ f \frac{y^W}{z^W} + v_o \end{bmatrix}, \quad \mathbf{p}_R = \begin{bmatrix} u_R \\ v_R \end{bmatrix} = \begin{bmatrix} f \frac{x^W}{z^W} + u_o - f \frac{T_c}{2z^W} \\ f \frac{y^W}{z^W} + v_o \end{bmatrix}. \quad (27)$$

The relationship between disparity d and depth z^W is as follows [29]:

$$d = u_L - u_R = f \frac{T_c}{z^W}, \quad (28)$$

where it can be observed that d is inversely proportional to z^W . Therefore, for a distant 3D point \mathbf{p}^W , \mathbf{p}_L and \mathbf{p}_R are close to each other. On the other hand, when \mathbf{p}^W is lying near the stereo rig, the position difference between \mathbf{p}_L and \mathbf{p}_R is large. Therefore, disparity estimation can be regarded as a task of 1) finding the correspondence (\mathbf{p}_L and \mathbf{p}_R) pairs, which are on the same image row, between the left and right images and 2) producing two disparity images \mathbf{D}_L and \mathbf{D}_R , as shown in Fig. 11.

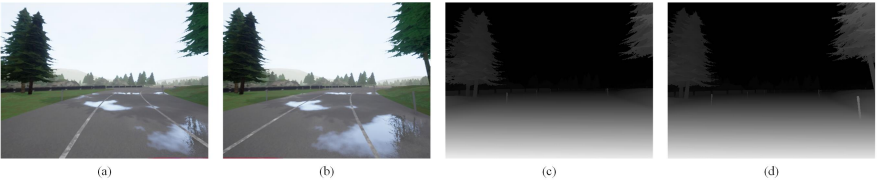


Fig. 11 (a) left image, (b) right image, (c) left disparity image \mathbf{D}_L and (d) right disparity image \mathbf{D}_R .

4.3.3 Disparity Estimation

The two key aspects of computer stereo vision are speed and accuracy [67]. Over the past two decades, a lot of research has been carried out to improve both the

disparity precision and the algorithm's computational complexity. However, the stereo vision algorithms designed to achieve better disparity accuracy typically have higher computational complexity [29]. Hence, speed and precision are two desirable but conflicting properties, and it is very challenging to achieve both of them simultaneously [67].

In general, the main motivation of designing a stereo vision algorithm is to improve the trade-off between speed and accuracy. In most circumstances, a desirable trade-off entirely depends on the target application [67]. For instance, a real-time performance is required for the stereo vision systems applied in autonomous driving, because other systems, such as data-fusion semantic driving scene segmentation, usually take up only a small portion of the processing time, and can be easily implemented in real-time if the 3D information is available [29]. Although the execution time of a stereo vision system can definitely be reduced with future advances in hardware computational power, the improvements on the algorithm itself are also very important [67].

The state-of-the-art stereo vision algorithms can be classified as either computer vision-based or machine/deep learning-based. The former typically formulates disparity estimation as a local block matching problem or a global energy minimization problem [66], while the latter basically considers disparity estimation as a binary classification/regression problem and learns a probability distribution over all disparity values [68].

Computer vision-based stereo vision algorithms

The computer vision-based disparity estimation algorithms are categorized as: 1) local, 2) global and 3) semi-global [69]. The local algorithms simply select an image block from the left image and match it with a series of image blocks selected from the right image. The best disparities correspond to either the lowest difference costs or the highest correlation costs. On the other hand, the global algorithms translate disparity estimation into a probability maximization problem or an energy minimization problem [70], which can be solved using Markov random field (MRF)-based optimization algorithms [71]. Semi-global matching (SGM) [72] approximates the MRF inference by performing cost aggregation along all directions in the image, which has greatly improved both the accuracy and efficiency of disparity estimation. Generally, a computer vision-based disparity estimation algorithm consists of four main steps: 1) cost computation, 2) cost aggregation, 3) disparity optimization and 4) disparity refinement [73].

1. Cost computation

The disparity d is a random variable with N possible discrete states, each of which is associated with a matching cost c . The two most commonly used pixel-wise matching costs are the absolute difference (AD) cost c_{AD} and the squared difference (SD) cost c_{SD} [73]. Since the left and right images are typically in gray-scale format, c_{AD} and c_{SD} can be computed using [74]:

$$\begin{aligned} c_{\text{AD}}(\mathbf{p}, d) &= |i_{\text{L}}(\mathbf{p}) - i_{\text{R}}(\mathbf{p} - \mathbf{d})|, \\ c_{\text{SD}}(\mathbf{p}, d) &= (i_{\text{L}}(\mathbf{p}) - i_{\text{R}}(\mathbf{p} - \mathbf{d}))^2, \end{aligned} \quad (29)$$

where $\mathbf{d} = [d, 0]^\top$, $i_{\text{L}}(\mathbf{p})$ denotes the pixel intensity of $\mathbf{p} = [u, v]^\top$ in the left image and $i_{\text{R}}(\mathbf{p} - \mathbf{d})$ represents the pixel intensity of $\mathbf{p} - \mathbf{d} = [u - d, v]^\top$ in the right image.

2. Cost aggregation

In order to minimize the incorrect matches, the pixel-wise difference costs are often aggregated over all pixels within a support region [69]:

$$c_{\text{agg}}(\mathbf{p}, d) = w(\mathbf{p}, d) * C(\mathbf{p}, d), \quad (30)$$

where the center of the support region is at $\mathbf{p} = [u, v]^\top$; the corresponding disparity is d ; c_{agg} denotes the aggregated cost; w is a kernel that represents the support region; C represents a neighborhood system containing the pixel-wise matching costs of all pixels within the support region. c_{agg} can be obtained by performing a convolution between w and C . A large support region can help reduce the ambiguities for disparity optimization, but it will also increase the algorithm execution time significantly.

Since the support regions are always rectangular blocks, these algorithms are also known as *stereo block matching* [66]. When the convolution process is a box blurring (all the elements in w are 1), the aggregations of c_{AD} and c_{SD} are referred to as the sum of absolute difference (SAD) and the sum of squared difference (SSD), respectively, which can be written as [29]:

$$\begin{aligned} c_{\text{SAD}}(\mathbf{p}, d) &= \sum_{\mathbf{q} \in \mathcal{N}_{\mathbf{p}}} |i_{\text{L}}(\mathbf{q}) - i_{\text{R}}(\mathbf{q} - \mathbf{d})|, \\ c_{\text{SSD}}(\mathbf{p}, d) &= \sum_{\mathbf{q} \in \mathcal{N}_{\mathbf{p}}} (i_{\text{L}}(\mathbf{q}) - i_{\text{R}}(\mathbf{q} - \mathbf{d}))^2, \end{aligned} \quad (31)$$

where $\mathcal{N}_{\mathbf{p}}$ is the support region (or neighborhood system) of \mathbf{p} . Although the SAD and the SSD are computationally efficient, they are very sensitive to the intensity difference. In this regard, some other cost functions, such as the normalized cross-correlation (NCC), are more prevalently used for cost computation and aggregation. The cost function of the NCC is as follows [66]:

$$c_{\text{NCC}}(\mathbf{p}, d) = \frac{1}{n\sigma_L\sigma_R} \sum_{\mathbf{q} \in \mathcal{N}_{\mathbf{p}}} (i_L(\mathbf{q}) - \mu_L)(i_R(\mathbf{q} - \mathbf{d}) - \mu_R), \quad (32)$$

where

$$\sigma_L = \sqrt{\sum_{\mathbf{q} \in \mathcal{N}_{\mathbf{p}}} (i_L(\mathbf{q}) - \mu_L)^2 / n}, \quad \sigma_R = \sqrt{\sum_{\mathbf{q} \in \mathcal{N}_{\mathbf{p}}} (i_R(\mathbf{q} - \mathbf{d}) - \mu_R)^2 / n}, \quad (33)$$

μ_L and μ_R represent the means of the pixel intensities within the left and right image block, respectively; σ_L and σ_R denote the standard deviations of the left and right image blocks, respectively; n represents the number of pixels within each image blocks. The NCC cost $c_{\text{NCC}} \in [-1, 1]$ reflects the similarity between the given pair of left and right image blocks. Therefore, a higher c_{NCC} corresponds to a better block matching.

In addition to the cost aggregation via box blurring, many adaptive cost aggregation strategies have been proposed to improve disparity accuracy. One of the most famous algorithms is fast bilateral stereo (FBS) [75, 76], which uses a bilateral filter to aggregate the matching costs adaptively. A general expression of cost aggregation in FBS is as follows [77]:

$$c_{\text{agg}}(\mathbf{p}, d) = \frac{\sum_{\mathbf{q} \in \mathcal{N}_{\mathbf{q}}} \omega_d(\mathbf{q})\omega_r(\mathbf{q})c(\mathbf{q}, d)}{\sum_{\mathbf{q} \in \mathcal{N}_{\mathbf{q}}} \omega_d(\mathbf{q})\omega_r(\mathbf{q})}, \quad (34)$$

where ω_d and ω_r are based on the spatial distance and the color similarity, respectively [76]. The costs c within a rectangular block are aggregated adaptively to produce c_{agg} .

3. Disparity Optimization

The local algorithms simply select the shifting distances that correspond to the lowest difference costs or the highest correlation costs as the best disparities. This optimization technique is also known as winner-take-all (WTA).

Unlike the principle of the WTA applied in the local algorithms, the matching costs from neighboring pixels are also taken into account in the global algorithms,

e.g., graph cuts (GC) [78] and belief propagation (BP) [79]. The MRF is a commonly used graphical model in these global algorithms. An example of the MRF model is depicted in Fig. 12. The graph $\mathcal{G} = (\mathcal{P}, \mathcal{E})$ is a set of vertices \mathcal{P} connected by edges \mathcal{E} , where $\mathcal{P} = \{\mathbf{p}_{11}, \mathbf{p}_{12}, \dots, \mathbf{p}_{mn}\}$ and $\mathcal{E} = \{(\mathbf{p}_{ij}, \mathbf{p}_{st}) \mid \mathbf{p}_{ij}, \mathbf{p}_{st} \in \mathcal{P}\}$. Two edges sharing one common vertex are called a pair of adjacent edges [80]. Since the MRF is considered to be undirected, $(\mathbf{p}_{ij}, \mathbf{p}_{st})$ and $(\mathbf{p}_{st}, \mathbf{p}_{ij})$ refer to the same edge here. $\mathcal{N}_{ij} = \{\mathbf{q}_{1_{\mathbf{p}_{ij}}}, \mathbf{q}_{2_{\mathbf{p}_{ij}}}, \dots, \mathbf{q}_{k_{\mathbf{p}_{ij}}} \mid \mathbf{q}_{\mathbf{p}_{ij}} \in \mathcal{P}\}$ is a neighborhood system of \mathbf{p}_{ij} .

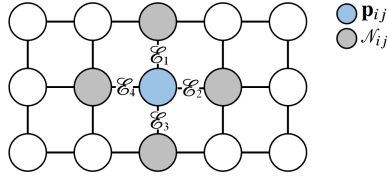


Fig. 12 MRF model.

For stereo vision problems, \mathcal{P} is a $m \times n$ disparity image and \mathbf{p}_{ij} is a vertex (or node) at the site of (i, j) with a label of disparity d_{ij} . Because more candidates taken into consideration usually make the inference of a true disparity intractable, only the neighbors adjacent to \mathbf{p}_{ij} are considered for stereo matching [71]. This is also known as a pairwise MRF. The disparity of \mathbf{p}_{ij} tends to have a strong correlation with its vicinities, while it is linked implicitly to any other random nodes in the disparity map. The joint probability of the MRF is written as [71]:

$$P(\mathbf{p}, q) = \prod_{\mathbf{p}_{ij} \in \mathcal{P}} \Phi(\mathbf{p}_{ij}, q_{\mathbf{p}_{ij}}) \prod_{\mathbf{q}_{\mathbf{p}_{ij}} \in \mathcal{N}_{ij}} \Psi(\mathbf{p}_{ij}, \mathbf{q}_{\mathbf{p}_{ij}}), \quad (35)$$

where $q_{\mathbf{p}_{ij}}$ represents the intensity differences, $\Phi(\cdot)$ expresses the compatibility between possible disparities and the corresponding intensity differences, and $\Psi(\cdot)$ expresses the compatibility between \mathbf{p}_{ij} and its neighborhood system. Now, the aim of finding the best disparity is equivalent to maximizing the probability in (35). This can be realized by formulating (35) as an energy function [62]:

$$E(\mathbf{p}) = \sum_{\mathbf{p}_{ij} \in \mathcal{P}} D(\mathbf{p}_{ij}, q_{\mathbf{p}_{ij}}) + \sum_{\mathbf{q}_{\mathbf{p}_{ij}} \in \mathcal{N}_{ij}} V(\mathbf{p}_{ij}, \mathbf{q}_{\mathbf{p}_{ij}}), \quad (36)$$

where $D(\cdot)$ and $V(\cdot)$ are two energy functions. $D(\cdot)$ corresponds to the matching cost and $V(\cdot)$ determines the aggregation from the neighbors. In the MRF model, the method to formulate an adaptive $V(\cdot)$ is important, because the intensity in

discontinuous areas usually varies greatly from that of its neighbors [29]. However, the process of minimizing (36) results in high computational complexities, making real-time performance challenging. Therefore, SGM [72] breaks down (36) into:

$$E(\mathbf{D}) = \sum_{\mathbf{p}} \left(c(\mathbf{p}, d_{\mathbf{p}}) + \sum_{\mathbf{q} \in \mathcal{N}_{\mathbf{p}}} \lambda_1 \delta(|d_{\mathbf{p}} - d_{\mathbf{q}}| = 1) + \sum_{\mathbf{q} \in \mathcal{N}_{\mathbf{p}}} \lambda_2 \delta(|d_{\mathbf{p}} - d_{\mathbf{q}}| > 1) \right), \quad (37)$$

where \mathbf{D} is the disparity image, c is the matching cost, \mathbf{q} is a pixel in the neighborhood system $\mathcal{N}_{\mathbf{p}}$ of \mathbf{p} . λ_1 penalizes the neighboring pixels with small disparity differences, *i.e.*, one pixel; λ_2 penalizes the neighboring pixels with large disparity differences, *i.e.*, larger than one pixel. $\delta(\cdot)$ returns 1 if its argument is true and 0 otherwise.

4. Disparity Refinement

The disparity refinement process usually involves several post-processing steps, such as the left-and-right disparity consistency check (LRDCC), subpixel enhancement and weighted median filtering [81]. The LRDCC can remove most of the occluded areas, which are only visible in one image [66]. In addition, a disparity error larger than one pixel may result in a non-negligible difference in the 3D geometry reconstruction result [66]. Therefore, subpixel enhancement provides an easy way to increase the resolution of the disparity image by simply interpolating the matching costs around the initial disparity [81]. Moreover, a median filter is always applied to the disparity image to fill the holes and remove the incorrect matches [81]. However, the above disparity refinement algorithms are not always necessary and the sequential use of these steps depends entirely on the chosen algorithm.

Machine/deep learning-based stereo vision algorithms

With recent advances in machine/deep learning, CNNs have been prevalently used for disparity estimation. For instance, Žbontar and LeCun [82] utilized a CNN to compute patch-wise similarity scores, as shown in Fig. 13, which consists of a convolutional layer L_1 and seven fully-connected layers L_2 - L_8 . The inputs to this CNN are two 9×9 pixels gray-scale image patches. L_1 consists of 32 kernels of size $5 \times 5 \times 1$. L_2 and L_3 have 200 neurons each. After L_3 the two 200-dimensional vectors are concatenated into a 400-dimensional vector and

passed through L_4 - L_7 . L_8 projects the output of L_7 into two real numbers, which are then fed through a softmax function to produce a distribution over the two classes: a) good match and b) bad match. Finally, they utilize computer vision-based cost aggregation and disparity optimization/refinement techniques to produce disparity images. Although this method has achieved the state-of-the-art accuracy, it is limited by the traditional cost aggregation technique and can produce wrong predictions in occluded or texture-less/reflective regions [83].

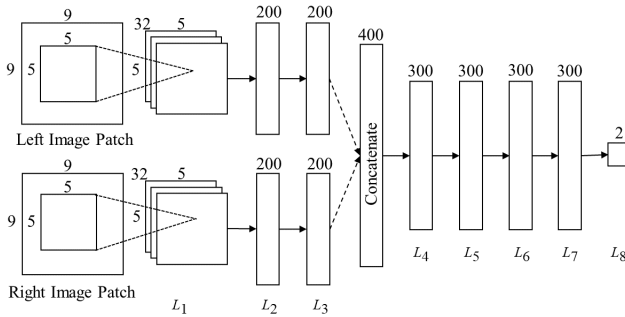


Fig. 13 The architecture of the CNN proposed in [82].

In this regard, some researchers have leveraged CNNs to improve computer vision-based cost aggregation step. SGM-Nets [84] is one of the most well-known methods of this type. Its main contribution is a CNN-based technique for predicting SGM penalty parameters λ_1 and λ_2 in (37) [72], as illustrated in Fig. 14. A 5×5 pixels gray-scale image patch and its normalized position are used as the inputs of the CNN, which has a) two convolution layers, with a rectified linear unit (ReLU) layer after each of them; b) a concatenate layer for merging the two types of inputs; c) two fully connected (FC) layers of size 128 each, with a ReLU layer and an exponential linear unit (ELU) after them, respectively; d) a constant layer to keep SGM penalty values positive. The costs can then be accumulated along four directions. The network’s output values correspond to standard parameterization.

Recently, end-to-end deep CNNs have become very popular. For example, Mayer *et al.* [85] created three large synthetic datasets⁵ (FlyingThings3D, Driving and Monkaa) and proposed a CNN named DispNet for dense disparity estimation. Later on, Pang *et al.* [86] proposed a two-stage cascade CNN for disparity estimation, where the first stage advances DispNet [85] by equipping it

⁵ mb.informatik.uni-freiburg.de/resources/datasets/SceneFlowDatasets.en.html

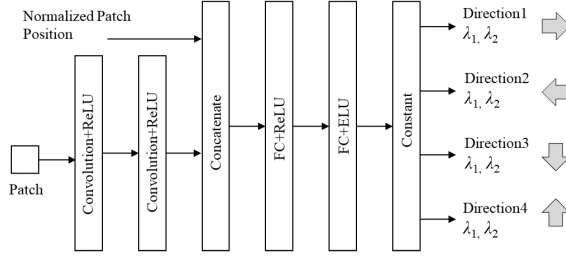


Fig. 14 The architecture of SGM-Nets [84].

with extra up-convolution modules and the second stage rectifies the disparity initialized by the first stage and generates residual signals across multiple scales. Furthermore, GCNet [87] incorporated feature extraction (cost computation), cost aggregation and disparity optimization/refinement into a single end-to-end CNN model, and it achieved the state-of-the-art accuracy on the FlyingThings3D benchmark [85] as well as the KITTI stereo 2012 and 2015 benchmarks [88–90]. In 2018, Chang *et al.* [91] proposed pyramid stereo matching network (PSMNet), which consists of two modules: a) spatial pyramid pooling and b) 3D CNN. The former aggregates the context in different scales and locations, while the latter regularizes the cost volume. Different from PSMNet [91], guided aggregation net (GANet) [83] replaces the widely used 3D CNN with two novel layers, a semi-global aggregation layer and a local guided aggregation layer, which help save a lot of memory and computational cost.

Although the aforementioned CNN-based disparity estimation methods have achieved compelling results, they usually have a huge number of learnable parameters, resulting in a long processing time. Therefore, current state-of-the-art CNN-based disparity estimation algorithms have been merely put into practical uses in autonomous driving. We believe these methods will be applied in more real-world applications with future advances in hardware computational power.

4.3.4 Performance Evaluation

As discussed above, speed and accuracy are two key properties and they are always pitted against each other, and therefore, the performance evaluation of a given stereo vision algorithm usually involves both of these two properties [67].

The following two metrics are commonly used to evaluate the accuracy of an estimated disparity image [92]:

1. Root mean squared (RMS) error e_{RMS} :

$$e_{\text{RMS}} = \sqrt{\frac{1}{N} \sum_{\mathbf{p} \in \mathcal{P}} |\mathbf{D}_{\text{E}}(\mathbf{p}) - \mathbf{D}_{\text{G}}(\mathbf{p})|^2}, \quad (38)$$

2. Percentage of error pixels (PEP) e_{PEP} (threshold: δ_d pixels):

$$e_{\text{PEP}} = \frac{1}{N} \sum_{\mathbf{p} \in \mathcal{P}} \delta(|\mathbf{D}_{\text{E}}(\mathbf{p}) - \mathbf{D}_{\text{G}}(\mathbf{p})| > \delta_d) \times 100\%, \quad (39)$$

where \mathbf{D}_{E} and \mathbf{D}_{G} represent the estimated and ground truth disparity images, respectively; N denotes the total number of disparities used for evaluation; δ_d represents the disparity evaluation tolerance.

Additionally, a general way to depict the efficiency of an algorithm is given in millions of disparity evaluations per second Mde/s [67] as follows:

$$\text{Mde/s} = \frac{u_{\max} v_{\max} d_{\max}}{t} 10^{-6}. \quad (40)$$

However, the speed of a disparity estimation algorithm typically varies across different platforms, and it can be greatly boosted by exploiting the parallel computing architecture.

5 Heterogeneous Computing

Heterogeneous computing refers to the systems that use multiple types of processors or cores. In the past, heterogeneous computing meant for different instruction-set architectures (ISAs) had to be handled differently, while the modern heterogeneous system architecture (HSA) systems allow the users to utilize multiple processor types. As illustrated in Fig. 15, a typical HSA system con-

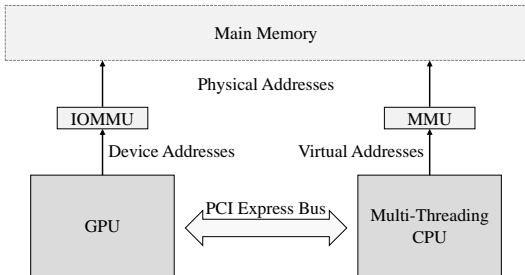


Fig. 15 Heterogeneous system architecture.

sists of two different types of processors: 1) a multi-threading central processing

unit (CPU) and 2) a graphics processing unit (GPU) [93], which are connected by a peripheral component interconnect (PCI) express bus. The CPU's memory management unit (MMU) and the GPU's input/output memory management unit (IOMMU) comply with the HSA hardware specifications. CPU runs the operating system and performs traditional serial tasks, while GPU performs 3D graphics rendering and CNN training.

5.1 Multi-Threading CPU

The application programming interface (API) open multi-processing (OpenMP) is typically used to break a serial code into independent chunks for parallel processing, and it supports multi-platform shared-memory multiprocessing programming in C/C++ and Fortran [94]. An explicit parallelism programming model, typically known as a fork-join model, is illustrated in Fig. 16, where the

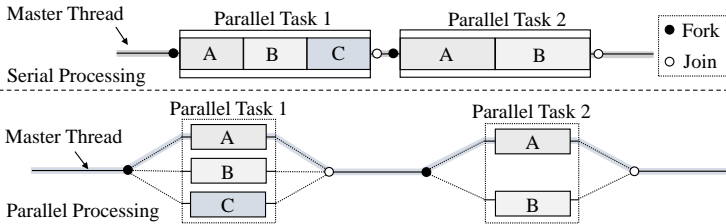


Fig. 16 Serial processing vs. parallel processing.

compiler instructs a section of the serial code to run in parallel [95]. The master thread (serial execution on one core) forks a number of slave threads. The tasks are divided to run in parallel amongst the slave threads on multiple cores. Synchronization waits until all slave threads finish their allocated tasks [57]. Finally, the slave threads join together at a subsequent point and resume sequential execution.

5.2 GPU

GPUs have been extensively used in computer vision and deep learning to accelerate the computationally intensive but parallelly-efficient processing and CNN training. Compared with a CPU which consists of a low number of cores op-

timized for sequentially serial processing, the GPU has a highly parallel architecture which is composed of hundreds or thousands of lighter cores to handle multiple tasks concurrently.

A typical architecture of GPU is shown in Fig. 17, which consists of N streaming multi-processors with M streaming processors (CUDA cores) on each of them. The single instruction multiple data (SIMD) architecture allows the SPs on the same SM to execute the same instruction but process different data at each clock cycle. The device has its own dynamic random access memory (DRAM) which consists of global memory, constant memory and texture memory. The latter can communicate with the host memory via the graphical/memory controller hub (GMCH) and the I/O controller hub (ICH) which are also known as the Intel northbridge and the Intel southbridge, respectively. Each SM has four types of on-chip memories: register, shared memory, constant cache and texture cache. Since they are on-chip memories, the constant cache and texture cache are utilized to speed up the data fetching from the constant memory and texture memory, respectively. Due to the fact that the shared memory is small, it is used for the duration of processing a block. The register is only visible to the thread. The details of different types of memories are illustrated in Table 5.2.

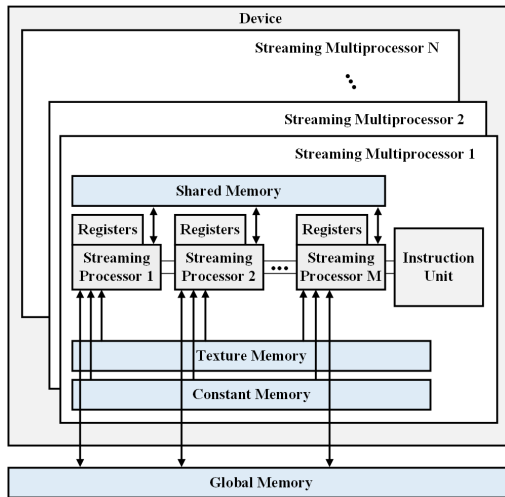


Fig. 17 GPU architecture [76].

In CUDA C programming, the threads are grouped into a set of 3D thread blocks which are then organized as a 3D grid. The kernels are defined on the host using the CUDA C programming language. Then, the host issues the commands that submit the kernels to devices for execution. Only one kernel can be executed

Table 1 GPU memory architecture [96].

Memory	Location	Cached	Access	Scope
register	on-chip	n/a	r/w	one thread
shared	on-chip	n/a	r/w	all threads in a block
global	off-chip	no	r/w	all threads + host
constant	off-chip	yes	r	all threads + host
texture	off-chip	yes	r	all threads + host

at a given time. Once a thread block is distributed to an SM, the threads are divided into groups of 32 parallel threads which are executed by SPs. Each group of 32 parallel threads is known as a warp. Therefore, the size of a thread block is usually chosen as a multiple of 32 to ensure efficient data processing.

6 Summary

In this chapter, we first introduced the autonomous car system, from both hardware aspect (car sensors and car chassis) and software aspect (perception, localization and mapping, prediction and planning, and control). Particularly, we introduced the autonomous car perception module, which has four main functionalities: 1) visual feature detection, description and matching, 2) 3D information acquisition, 3) object detection/recognition and 4) semantic image segmentation. Later on, we provided readers with the preliminaries for the epipolar geometry and introduced computer stereo vision from theory to algorithms. Finally, heterogeneous computing architecture, consisting of a multi-threading CPU and a GPU, was introduced.

References

1. R. Fan, J. Jiao, H. Ye, Y. Yu, I. Pitas, and M. Liu, “Key ingredients of self-driving cars,” 2019.
2. I. Pitas, *Digital image processing algorithms and applications*. John Wiley & Sons, 2000.
3. “Lidar—light detection and ranging—is a remote sensing method used to examine the surface of the earth,” *NOAA. Archived from the original on*, vol. 4, 2013.
4. T. Bureau, “Radar definition,” *Public Works and Government Services Canada*, 2013.
5. W. J. Westerveld, “Silicon photonic micro-ring resonators to sense strain and ultrasound,” 2014.

6. L. Zheng, Y. Zhu, B. Xue, M. Liu, and R. Fan, "Low-cost gps-aided lidar state estimation and map building," in *2019 IEEE International Conference on Imaging Systems and Techniques (IST)*. IEEE, 2019, pp. 1–6.
7. N. Samama, *Global positioning: Technologies and performance*. John Wiley & Sons, 2008, vol. 7.
8. S. Liu, "Chassis technologies for autonomous robots and vehicles," 2019.
9. M. U. M. Bhutta, M. Kuse, R. Fan, Y. Liu, and M. Liu, "Loop-box: Multiagent direct slam triggered by single loop closure for large-scale mapping," *IEEE transactions on cybernetics*, 2020.
10. R. C. Smith and P. Cheeseman, "On the representation and estimation of spatial uncertainty," *The international journal of Robotics Research*, vol. 5, no. 4, pp. 56–68, 1986.
11. C. Katrakazas, M. Quddus, W.-H. Chen, and L. Deka, "Real-time motion planning methods for autonomous on-road driving: State-of-the-art and future research directions," *Transportation Research Part C: Emerging Technologies*, vol. 60, pp. 416–442, 2015.
12. T. H. Cormen, "Section 24.3: Dijkstra's algorithm," *Introduction to algorithms*, pp. 595–601, 2001.
13. D. Delling, P. Sanders, D. Schultes, and D. Wagner, "Engineering route planning algorithms," in *Algorithmics of large and complex networks*. Springer, 2009, pp. 117–139.
14. M. Willis, "Proportional-integral-derivative control," *Dept. of Chemical and Process Engineering University of Newcastle*, 1999.
15. G. C. Goodwin, S. F. Graebe, M. E. Salgado *et al.*, *Control system design*. Upper Saddle River, NJ: Prentice Hall, 2001.
16. C. E. Garcia, D. M. Prett, and M. Morari, "Model predictive control: theory and practice—a survey," *Automatica*, vol. 25, no. 3, pp. 335–348, 1989.
17. M. Hassaballah, A. A. Abdelmegeid, and H. A. Alshazly, "Image features detection, description and matching," in *Image Feature Detectors and Descriptors*. Springer, 2016, pp. 11–45.
18. S. Liu and X. Bai, "Discriminative features for image classification and retrieval," *Pattern Recognition Letters*, vol. 33, no. 6, pp. 744–751, 2012.
19. P. Moreels and P. Perona, "Evaluation of features detectors and descriptors based on 3d objects," *International journal of computer vision*, vol. 73, no. 3, pp. 263–284, 2007.
20. P. Dollar, C. Wojek, B. Schiele, and P. Perona, "Pedestrian detection: An evaluation of the state of the art," *IEEE transactions on pattern analysis and machine intelligence*, vol. 34, no. 4, pp. 743–761, 2011.
21. M. Danelljan, G. Häger, F. S. Khan, and M. Felsberg, "Discriminative scale space tracking," *IEEE transactions on pattern analysis and machine intelligence*, vol. 39, no. 8, pp. 1561–1575, 2016.
22. D. G. Lowe, "Distinctive image features from scale-invariant keypoints," *International journal of computer vision*, vol. 60, no. 2, pp. 91–110, 2004.
23. H. Bay, T. Tuytelaars, and L. Van Gool, "Surf: Speeded up robust features," in *European conference on computer vision*. Springer, 2006, pp. 404–417.
24. E. Rublee, V. Rabaud, K. Konolige, and G. Bradski, "Orb: An efficient alternative to sift or surf," in *2011 International conference on computer vision*. Ieee, 2011, pp. 2564–2571.
25. S. Leutenegger, M. Chli, and R. Y. Siegwart, "Brisk: Binary robust invariant scalable keypoints," in *2011 International conference on computer vision*. Ieee, 2011, pp. 2548–2555.

26. R. Hartley and A. Zisserman, *Multiple view geometry in computer vision*. Cambridge university press, 2003.
27. H. Wang, R. Fan, and M. Liu, “Cot-amflow: Adaptive modulation network with co-teaching strategy for unsupervised optical flow estimation,” 2020.
28. S. Ullman, “The interpretation of structure from motion,” *Proceedings of the Royal Society of London. Series B. Biological Sciences*, vol. 203, no. 1153, pp. 405–426, 1979.
29. R. Fan, “Real-time computer stereo vision for automotive applications,” Ph.D. dissertation, University of Bristol, 2018.
30. B. Triggs, P. F. McLauchlan, R. I. Hartley, and A. W. Fitzgibbon, “Bundle adjustment—a modern synthesis,” in *International workshop on vision algorithms*. Springer, 1999, pp. 298–372.
31. H. Wang, Y. Liu, H. Huang, Y. Pan, W. Yu, J. Jiang, D. Lyu, M. J. Bocus, M. Liu, I. Pitas *et al.*, “Atg-pvd: Ticketing parking violations on a drone,” 2020.
32. Z.-Q. Zhao, P. Zheng, S.-t. Xu, and X. Wu, “Object detection with deep learning: A review,” *IEEE transactions on neural networks and learning systems*, vol. 30, no. 11, pp. 3212–3232, 2019.
33. D. Wang, C. Devin, Q.-Z. Cai, F. Yu, and T. Darrell, “Deep object-centric policies for autonomous driving,” in *2019 International Conference on Robotics and Automation (ICRA)*. IEEE, 2019, pp. 8853–8859.
34. A. Mogelmoose, M. M. Trivedi, and T. B. Moeslund, “Vision-based traffic sign detection and analysis for intelligent driver assistance systems: Perspectives and survey,” *IEEE Transactions on Intelligent Transportation Systems*, vol. 13, no. 4, pp. 1484–1497, 2012.
35. B. Wu, F. Iandola, P. H. Jin, and K. Keutzer, “Squeezedet: Unified, small, low power fully convolutional neural networks for real-time object detection for autonomous driving,” in *Proceedings of the IEEE Conference on Computer Vision and Pattern Recognition Workshops*, 2017, pp. 129–137.
36. R. Girshick, J. Donahue, T. Darrell, and J. Malik, “Rich feature hierarchies for accurate object detection and semantic segmentation,” in *Proceedings of the IEEE conference on computer vision and pattern recognition*, 2014, pp. 580–587.
37. R. Girshick, “Fast r-cnn,” in *Proceedings of the IEEE international conference on computer vision*, 2015, pp. 1440–1448.
38. S. Ren, K. He, R. Girshick, and J. Sun, “Faster r-cnn: Towards real-time object detection with region proposal networks,” in *Advances in neural information processing systems*, 2015, pp. 91–99.
39. J. Redmon, S. Divvala, R. Girshick, and A. Farhadi, “You only look once: Unified, real-time object detection,” in *Proceedings of the IEEE conference on computer vision and pattern recognition*, 2016, pp. 779–788.
40. J. Redmon and A. Farhadi, “Yolov3: An incremental improvement,” 2018.
41. A. Bochkovskiy, C.-Y. Wang, and H.-Y. M. Liao, “Yolov4: Optimal speed and accuracy of object detection,” 2020.
42. R. Fan, H. Wang, P. Cai, and M. Liu, “Sne-roadseg: Incorporating surface normal information into semantic segmentation for accurate freespace detection,” in *European Conference on Computer Vision*. Springer, 2020, pp. 340–356.
43. H. Wang, R. Fan, Y. Sun, and M. Liu, “Applying surface normal information in drivable area and road anomaly detection for ground mobile robots,” 2020.

44. J. Long, E. Shelhamer, and T. Darrell, "Fully convolutional networks for semantic segmentation," in *Proceedings of the IEEE conference on computer vision and pattern recognition*, 2015, pp. 3431–3440.
45. O. Ronneberger, P. Fischer, and T. Brox, "U-net: Convolutional networks for biomedical image segmentation," in *International Conference on Medical image computing and computer-assisted intervention*. Springer, 2015, pp. 234–241.
46. V. Badrinarayanan, A. Kendall, and R. Cipolla, "Segnet: A deep convolutional encoder-decoder architecture for image segmentation," *IEEE transactions on pattern analysis and machine intelligence*, vol. 39, no. 12, pp. 2481–2495, 2017.
47. L.-C. Chen, Y. Zhu, G. Papandreou, F. Schroff, and H. Adam, "Encoder-decoder with atrous separable convolution for semantic image segmentation," in *Proceedings of the European conference on computer vision (ECCV)*, 2018, pp. 801–818.
48. M. Yang, K. Yu, C. Zhang, Z. Li, and K. Yang, "Denseaspp for semantic segmentation in street scenes," in *Proceedings of the IEEE Conference on Computer Vision and Pattern Recognition*, 2018, pp. 3684–3692.
49. Z. Tian, T. He, C. Shen, and Y. Yan, "Decoders matter for semantic segmentation: Data-dependent decoding enables flexible feature aggregation," in *Proceedings of the IEEE Conference on Computer Vision and Pattern Recognition*, 2019, pp. 3126–3135.
50. R. Fan, H. Wang, M. J. Bocus, and M. Liu, "We learn better road pothole detection: from attention aggregation to adversarial domain adaptation," *European Conference on Computer Vision (ECCV) Workshops*, 2020.
51. C. Hazirbas, L. Ma, C. Domokos, and D. Cremers, "Fusenet: Incorporating depth into semantic segmentation via fusion-based cnn architecture," in *Asian conference on computer vision*. Springer, 2016, pp. 213–228.
52. R. Fan, H. Wang, B. Xue, H. Huang, Y. Wang, M. Liu, and I. Pitas, "Three-filters-to-normal: An accurate and ultrafast surface normal estimator," 2020.
53. R. Fan, M. J. Bocus, and N. Dahnoun, "A novel disparity transformation algorithm for road segmentation," *Information Processing Letters*, vol. 140, pp. 18–24, 2018.
54. R. Fan, U. Ozgunalp, B. Hosking, M. Liu, and I. Pitas, "Pothole detection based on disparity transformation and road surface modeling," *IEEE Transactions on Image Processing*, vol. 29, pp. 897–908, 2019.
55. R. Fan and M. Liu, "Road damage detection based on unsupervised disparity map segmentation," *IEEE Transactions on Intelligent Transportation Systems*, 2019.
56. Q. Ha, K. Watanabe, T. Karasawa, Y. Ushiku, and T. Harada, "Mfnet: Towards real-time semantic segmentation for autonomous vehicles with multi-spectral scenes," in *2017 IEEE/RSJ International Conference on Intelligent Robots and Systems (IROS)*. IEEE, 2017, pp. 5108–5115.
57. R. Fan, V. Prokhorov, and N. Dahnoun, "Faster-than-real-time linear lane detection implementation using soc dsp tms320c6678," in *2016 IEEE International Conference on Imaging Systems and Techniques (IST)*. IEEE, 2016, pp. 306–311.
58. U. Ozgunalp, R. Fan, X. Ai, and N. Dahnoun, "Multiple lane detection algorithm based on novel dense vanishing point estimation," *IEEE Transactions on Intelligent Transportation Systems*, vol. 18, no. 3, pp. 621–632, 2016.
59. R. Fan and N. Dahnoun, "Real-time stereo vision-based lane detection system," *Measurement Science and Technology*, vol. 29, no. 7, p. 074005, 2018.

60. J. Jiao, R. Fan, H. Ma, and M. Liu, "Using dp towards a shortest path problem-related application," in *2019 International Conference on Robotics and Automation (ICRA)*. IEEE, 2019, pp. 8669–8675.
61. E. Trucco and A. Verri, *Introductory techniques for 3-D computer vision*. Prentice Hall Englewood Cliffs, 1998, vol. 201.
62. R. Fan, J. Jiao, J. Pan, H. Huang, S. Shen, and M. Liu, "Real-time dense stereo embedded in a uav for road inspection," in *Proceedings of the IEEE Conference on Computer Vision and Pattern Recognition (CVPR) Workshops*, 2019, pp. 535–543.
63. Z. Zhang, "A flexible new technique for camera calibration," *IEEE Transactions on pattern analysis and machine intelligence*, vol. 22, no. 11, pp. 1330–1334, 2000.
64. H. C. Longuet-Higgins, "A computer algorithm for reconstructing a scene from two projections," *Nature*, vol. 293, no. 5828, pp. 133–135, 1981.
65. R. I. Hartley, "In defense of the eight-point algorithm," *IEEE Transactions on pattern analysis and machine intelligence*, vol. 19, no. 6, pp. 580–593, 1997.
66. R. Fan, X. Ai, and N. Dahnoun, "Road surface 3d reconstruction based on dense subpixel disparity map estimation," *IEEE Transactions on Image Processing*, vol. 27, no. 6, pp. 3025–3035, 2018.
67. B. Tippetts, D. J. Lee, K. Lillywhite, and J. Archibald, "Review of stereo vision algorithms and their suitability for resource-limited systems," *Journal of Real-Time Image Processing*, vol. 11, no. 1, pp. 5–25, 2016.
68. W. Luo, A. G. Schwing, and R. Urtasun, "Efficient deep learning for stereo matching," in *Proceedings of the IEEE Conference on Computer Vision and Pattern Recognition*, 2016, pp. 5695–5703.
69. D. Scharstein and R. Szeliski, "High-accuracy stereo depth maps using structured light," in *2003 IEEE Computer Society Conference on Computer Vision and Pattern Recognition, 2003. Proceedings.*, vol. 1. IEEE, 2003, pp. I–I.
70. M. G. Mozerov and J. van de Weijer, "Accurate stereo matching by two-step energy minimization," *IEEE Transactions on Image Processing*, vol. 24, no. 3, pp. 1153–1163, 2015.
71. M. F. Tappen and W. T. Freeman, "Comparison of graph cuts with belief propagation for stereo, using identical mrf parameters," in *null*. IEEE, 2003, p. 900.
72. H. Hirschmuller, "Stereo processing by semiglobal matching and mutual information," *IEEE Transactions on pattern analysis and machine intelligence*, vol. 30, no. 2, pp. 328–341, 2007.
73. J. Žbontar and Y. LeCun, "Stereo matching by training a convolutional neural network to compare image patches," *The journal of machine learning research*, vol. 17, no. 1, pp. 2287–2318, 2016.
74. H. Hirschmuller and D. Scharstein, "Evaluation of stereo matching costs on images with radiometric differences," *IEEE transactions on pattern analysis and machine intelligence*, vol. 31, no. 9, pp. 1582–1599, 2008.
75. Q. Yang, L. Wang, R. Yang, H. Stewenius, and D. Nistér, "Stereo matching with color-weighted correlation, hierarchical belief propagation, and occlusion handling," *IEEE Transactions on Pattern Analysis and Machine Intelligence*, vol. 31, no. 3, pp. 492–504, 2008.
76. R. Fan, Y. Liu, M. J. Bocus, L. Wang, and M. Liu, "Real-time subpixel fast bilateral stereo," in *2018 IEEE International Conference on Information and Automation (ICIA)*. IEEE, 2018, pp. 1058–1065.

77. R. Fan, Y. Liu, X. Yang, M. J. Bocus, N. Dahnoun, and S. Tancock, "Real-time stereo vision for road surface 3-d reconstruction," in *2018 IEEE International Conference on Imaging Systems and Techniques (IST)*. IEEE, 2018, pp. 1–6.
78. Y. Boykov, O. Veksler, and R. Zabih, "Fast approximate energy minimization via graph cuts," *IEEE Transactions on pattern analysis and machine intelligence*, vol. 23, no. 11, pp. 1222–1239, 2001.
79. A. T. Ihler, A. S. Willsky *et al.*, "Loopy belief propagation: Convergence and effects of message errors," *Journal of Machine Learning Research*, vol. 6, no. May, pp. 905–936, 2005.
80. A. Blake, P. Kohli, and C. Rother, *Markov random fields for vision and image processing*. Mit Press, 2011.
81. D. Scharstein and R. Szeliski, "A taxonomy and evaluation of dense two-frame stereo correspondence algorithms," *International journal of computer vision*, vol. 47, no. 1-3, pp. 7–42, 2002.
82. J. Žbontar and Y. LeCun, "Computing the stereo matching cost with a convolutional neural network," in *Proceedings of the IEEE conference on computer vision and pattern recognition*, 2015, pp. 1592–1599.
83. F. Zhang, V. Prisacariu, R. Yang, and P. H. Torr, "Ga-net: Guided aggregation net for end-to-end stereo matching," in *Proceedings of the IEEE Conference on Computer Vision and Pattern Recognition*, 2019, pp. 185–194.
84. A. Seki and M. Pollefeys, "Sgm-nets: Semi-global matching with neural networks," in *Proceedings of the IEEE Conference on Computer Vision and Pattern Recognition*, 2017, pp. 231–240.
85. N. Mayer, E. Ilg, P. Hausser, P. Fischer, D. Cremers, A. Dosovitskiy, and T. Brox, "A large dataset to train convolutional networks for disparity, optical flow, and scene flow estimation," in *Proceedings of the IEEE conference on computer vision and pattern recognition*, 2016, pp. 4040–4048.
86. J. Pang, W. Sun, J. S. Ren, C. Yang, and Q. Yan, "Cascade residual learning: A two-stage convolutional neural network for stereo matching," in *Proceedings of the IEEE International Conference on Computer Vision Workshops*, 2017, pp. 887–895.
87. A. Kendall, H. Martirosyan, S. Dasgupta, P. Henry, R. Kennedy, A. Bachrach, and A. Bry, "End-to-end learning of geometry and context for deep stereo regression," in *Proceedings of the IEEE International Conference on Computer Vision*, 2017, pp. 66–75.
88. A. Geiger, P. Lenz, and R. Urtasun, "Are we ready for autonomous driving? the kitti vision benchmark suite," in *2012 IEEE Conference on Computer Vision and Pattern Recognition*. IEEE, 2012, pp. 3354–3361.
89. M. Menze, C. Heipke, and A. Geiger, "Joint 3d estimation of vehicles and scene flow." *ISPRS Annals of Photogrammetry, Remote Sensing & Spatial Information Sciences*, vol. 2, 2015.
90. C. Menze, Moritz; Heipke and A. Geiger, "Object scene flow," *ISPRS Journal of Photogrammetry and Remote Sensing*, vol. 140, pp. 60–76, 2018.
91. J.-R. Chang and Y.-S. Chen, "Pyramid stereo matching network," in *Proceedings of the IEEE Conference on Computer Vision and Pattern Recognition*, 2018, pp. 5410–5418.
92. J. L. Barron, D. J. Fleet, and S. S. Beauchemin, "Performance of optical flow techniques," *International journal of computer vision*, vol. 12, no. 1, pp. 43–77, 1994.

93. S. Mittal and J. S. Vetter, "A survey of cpu-gpu heterogeneous computing techniques," *ACM Computing Surveys (CSUR)*, vol. 47, no. 4, pp. 1–35, 2015.
94. H. Jin, D. Jespersen, P. Mehrotra, R. Biswas, L. Huang, and B. Chapman, "High performance computing using mpi and openmp on multi-core parallel systems," *Parallel Computing*, vol. 37, no. 9, pp. 562–575, 2011.
95. R. Fan, S. Duanmu, Y. Liu, Y. Zhu, J. Jiao, M. J. Bocus, Y. Yu, L. Wang, and M. Liu, "Real-time binocular vision implementation on an soc tms320c6678 dsp," in *International Conference on Computer Vision Systems*. Springer, 2019, pp. 13–23.
96. R. Fan and N. Dahnoun, "Real-time implementation of stereo vision based on optimised normalised cross-correlation and propagated search range on a gpu," in *2017 IEEE International Conference on Imaging Systems and Techniques (IST)*. IEEE, 2017, pp. 1–6.